CHEMISTRY OF MATERIALS

Article

pubs.acs.org/cm

Brittle Failure Mechanism in Thermoelectric Skutterudite $CoSb_3$

Guodong Li,[†,‡,§] Qi An,[⊥,§] Wenjuan Li,[†,‡] William A. Goddard, III,[*,⊥] Pengcheng Zhai,[†] Qingjie Zhang,[*,†] and G. Jeffrey Snyder[*,‡]

[†]State Key Laboratory of Advanced Technology for Materials Synthesis and Processing, Wuhan University of Technology, Wuhan, Hubei 430070, China

[‡]Department of Materials Science, Northwestern University, Evanston, Illinois 60208, United States

[⊥]Materials and Process Simulation Center, California Institute of Technology, Pasadena, California 91125, United States

Supporting Information

ABSTRACT: Skutterudites based on $CoSb_3$ have high thermoelectric efficiency, but the low fracture strength is a serious consideration for commercial applications. To understand the origin of the brittleness in $CoSb_3$, we examine the response along various shear and tensile deformations using density functional theory. We find that the Co−Sb bond dominates the ideal strength. Among all the shear and tensile deformation paths, shearing along the (001)/⟨100⟩ slip system has the lowest ideal strength, indicating it is the most likely slip system to be activated under pressure. We also find that, because the Sb−Sb covalent bond is softer than the Co−Sb bond, the Sb-rings are less rigid than the Co−Sb frameworks, which leads to the Sb-rings softening before the Co−Sb frameworks. Further deformation leads to deconstruction of Sb-rings and collapse of Co−Sb frameworks, resulting in structural failure. Moreover, we find that filling of the $CoSb_3$ void spaces with such typical fillers as Na, Ba, or Yb has little effect on the ideal strength and failure mode, which can be understood because they have little effect on the Sb-rings.

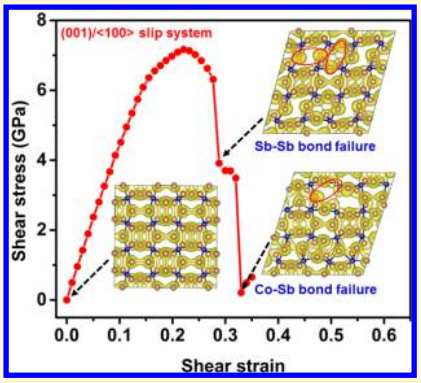

1. INTRODUCTION

Thermoelectric (TE) power generation devices are already important for such applications as powering space crafts for deep-space missions. Now, because they can directly convert heat into electricity with high reliability and no moving parts, they are being considered for recovery of automobile exhaust heat.[1] High efficiency of thermal-to-electrical energy conversion is necessary to advance such applications of thermoelectrics.[2−5] n-Type filled skutterudite based on $CoSb_3$ is recognized as one of the most promising TE materials since it has an excellent TE figure of merit ($zT > 1$).[6−10] However, engineering applications of $CoSb_3$ presents challenges. For example, the thermal expansion difference between the $CoSb_3$ TE material and the metal joints can easily result in significant thermo-mechanical stresses, leading to cracks close to the interface between the $CoSb_3$ and the joint metals.[11−13] Consequently, mechanical strength and toughness are of vital importance for the engineering applications of the skutterudite $CoSb_3$ material.

Because of its importance for engineering applications, the mechanical properties of $CoSb_3$ have been examined recently.[14−20] Rogl and Rogl reported experimental mechanical properties of doped skutterudite $CoSb_3$ such as elastic moduli, fracture toughness, and failure stress.[14] They showed that $CoSb_3$ has mechanical properties competitive with other TE materials. Ravi et al. focused on describing the elastic moduli, flexural strengths, and fracture toughness of advanced skutterudites materials.[15] Ruan et al. studied the low-cycle stress-controlled fatigue properties of $CoSb_3$-based skutterudite compounds in compression−compression fatigue.[16] Schmidt et al. reported temperature-dependent Young's modulus, shear modulus, and Poisson's ratio of p-type $Ce_{0.9}Fe_{3.5}Co_{0.5}Sb_{12}$ and n-type $Co_{0.95}Pd_{0.05}Te_{0.05}Sb_3$ skutterudite thermoelectric materials and found that the Young's and shear moduli decreased linearly with temperature.[17] Yang et al. used molecular dynamics simulations (Force field) to examine the stress−strain relationships of $CoSb_3$ and found it to be a typical brittle material.[18] Li et al. studied the tensile/compressive mechanical behavior of nanoporous skutterudite $CoSb_3$ thermoelectric material using molecular dynamics and found that elastic modulus of single crystalline $CoSb_3$ decreased with the increasing porosity.[19,20] However, the mechanism for brittle failure and the intrinsic mechanical properties of $CoSb_3$ remain unknown.

In order to determine the mechanism for brittle fracture in $CoSb_3$, we used density functional theory (DFT) at the Perdew−Burke−Ernzerhof (PBE) functional level to predict the tensile and shear deformation properties of single crystal $CoSb_3$. Here, we deformed along various lattice orientations until failure to shed lights on the intrinsic failure mechanism at the atomic scale. We found that the lowest ideal strength for $CoSb_3$ is along the (001)/⟨100⟩ slip system. This is because this leads to the smallest stretching of Co−Sb bond compared

Received: June 15, 2015
Revised: September 3, 2015
Published: September 4, 2015

DOI: 10.1021/acs.chemmater.5b02268
Chem. Mater. 2015, 27, 6329−6336

with other deformation systems. Due to the softer Sb−Sb covalent bond compared with Co−Sb bond, the rigidity of Sb-rings is weaker than that of Co−Sb frameworks, leading to softening of the Sb-rings before the Co−Sb frameworks. Further external deformation reveals that deconstruction of the Sb-rings and collapse of the Co−Sb frameworks result in structural failure. To examine the effects on the mechanics from filling, we added Na, Ba, and Yb atoms into the intrinsic cages of $CoSb_3$ but found no obvious effect on the ideal strength and failure mode of $CoSb_3$.

2. METHODOLOGY

Skutterudite $CoSb_3$ has the body centered cubic structure belonging to the I*m*3 (204) space group. Figure 1 shows the unit cell shifted by one-quarter distance along the body diagonal. It contains 8 Co atoms occupying the 8c-sites and 24 Sb atoms occupying the 24g-sites.[21] The Co atoms form a simple cubic framework within which 4 Sb atoms are arranged into a planar rectangular ring. There are 6 such rings in the unit cell, but two of the eight Co cubes are empty, giving rise to two cages (voids).

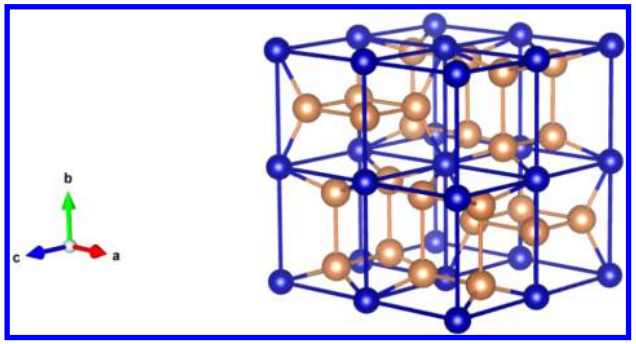

Figure 1. Co−Sb frameworks and Sb-rings in the cubic unit cell of $CoSb_3$. The Co and Sb atoms are represented with blue and brown balls, respectively.

All density functional theory (DFT) calculations were carried out using the Perdew−Burke−Ernzerhof (PBE) exchange-correlation functional with the projector augmented wave (PAW) method used to account for the core−valence interactions, and the Vienna *ab initio* Simulation Package (VASP) was used for all the calculations.[22−27] The convergence test showed that a plane wave cutoff energy of 500 eV gives good convergence for the total energies. A 7 × 7 × 7 Monkhorst−Pack uniform k-point reciprocal space sampling was adopted, and the convergence criteria were set to 1×10^{-6} eV energy difference for solving the electronic wave function and 1×10^{-2} eV/Å force for geometry optimization. Various DFT methods generally predict lattice parameters within a few percent of the experimental lattice parameters; our optimized lattice constant is a = 9.115 Å which is only 0.85% larger than the experimental value of 9.039 Å.[28] Our value using the PBE pseudopotential is consistent with the previous theoretical value of 9.14 Å using PBE.[29−31]

We achieved quasi-static mechanical loading of $CoSb_3$ by imposing the uniaxial tensile strain or shear strain on a particular direction while allowing structural relaxation along the other five strain components. The residual stresses for relaxation of these five strain directions are all less than 0.5 GPa.

To obtain stress−strain curves, a small uniaxial tensile or shear strain was applied sequentially to the supercell configuration relaxed in the previous step. We predefined a 1% level of strain as the small strain increment for each deformation step. At each deformation step, only the gamma k-point was sampled in the Brillouin zone for the supercells. The stress is defined as the force per deformed area, and the strain is defined as the true strain. This stress−strain curve was used to obtain the ideal shear and tensile strengths and to determine the fracture modes responsible for failure in $CoSb_3$. This relaxation method has been proved to be an effective tool to shed light on the intrinsic failure mechanism at the atomic scale.[22−24]

We considered three slip systems for the shear simulations:

- $(001)/\langle 100\rangle$ with (a, b, c) along $(\langle 100\rangle, \langle 010\rangle, \langle 001\rangle)$ using a supercell containing 128 atoms
- $(001)/\langle 110\rangle$ with (a, b, c) along $(\langle 110\rangle, \langle \bar{1}10\rangle, \langle 001\rangle)$ using a supercell containing 128 atoms
- $(111)/\langle 1\bar{1}0\rangle$ with (a, b, c) along $(\langle 1\bar{1}0\rangle, \langle 11\bar{2}\rangle, \langle 111\rangle)$ using a supercell containing 192 atoms

For tensile simulations, the deformation direction was along the a direction. Here, we obtained:

- $[100]$ oriented tensile mechanical behavior with (a, b, c) along $(\langle 100\rangle, \langle 010\rangle, \langle 001\rangle)$ with supercells containing 128 atoms
- $[1\bar{1}0]$ oriented tensile mechanical behavior with (a, b, c) along $(\langle 1\bar{1}0\rangle, \langle 11\bar{2}\rangle, \langle 111\rangle)$ with supercells containing 192 atoms
- $[111]$ oriented tensile mechanical behavior with (a, b, c) along $(\langle 111\rangle, \langle 1\bar{1}0\rangle, \langle 11\bar{2}\rangle)$ with supercells containing 192 atoms

3. RESULTS AND DISCUSSION

3.1. Elastic Properties of $CoSb_3$. We calculated the elastic mechanical parameters to validate our methodology. The elastic constants (C_{11}, C_{12}, C_{44}) were computed from stress−strain relationship as a function of various cell distortions δ from optimized structure. The Voigt-Reuss-Hill method was used to calculate the bulk modulus (B), shear modulus (G), Young's modulus (E), and poisson's ratio (v).[32] The predicted elastic mechanical properties (C_{11}, C_{12}, C_{44}, B, G, E, v) are listed in Table 1, which are consistent with experiments and previous *ab initio* results.[14,15,30,33,34] The small discrepancy of predicted results derives from the different convergence setup in VASP calculation.

3.2. Ideal Strength of $CoSb_3$. Figure 2 shows the shear and tensile stress responses as a function of applied strain, and Table 2 lists the corresponding mechanical qualities. Shearing along the $(001)/\langle 100\rangle$ slip system shows the lowest shear strength of 7.17 GPa with a failure strain of 0.288, which is most likely to be activated under pressure. Tension along the $[1\bar{1}0]$ direction shows the lowest tensile strength of 12.9 GPa with a failure strain of 0.184. All stresses increase with increasing strain until the ideal strength, indicating that the structure is strongly resistant to the deformations. Beyond the point of maximum stress, the curve generally decreases

Table 1. Predicted Elastic Constants (C_{11}, C_{12}, C_{44}), Bulk Modulus (B), Shear Modulus (G), Young's Modulus (E), and Poisson's Ratio (v) of $CoSb_3$ and Previous Experimental and Theoretical Data

	method	C_{11} (GPa)	C_{12} (GPa)	C_{44} (GPa)	B (GPa)	G (GPa)	E (GPa)	v
this work	*ab initio* (PBE)	187.07	37.53	50.97	87.38	59.45	145.38	0.223
refs 14 and 15	Expt	158.0		61	90	61	148	0.22−0.29
ref 33	Expt	164.0		59.0				
ref 34	*ab initio* (PBE)	182	37	50	85			
ref 30	*ab initio* (PBE)	172.0	43.7	57.7				

DOI: 10.1021/acs.chemmater.5b02268
Chem. Mater. 2015, 27, 6329−6336

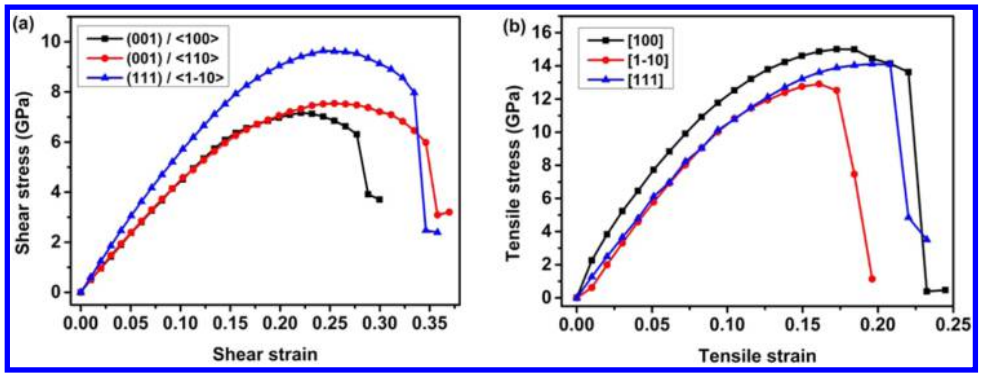

Figure 2. Calculated stress vs strain of $CoSb_3$ under different directions of (a) shear and (b) tension loads.

Table 2. Ideal Strength and Fracture Strain under Shear and Tensile Loadings

	shear			tension		
mechanics	(001)/⟨100⟩	(001)/⟨110⟩	(111)/⟨1$\bar{1}$0⟩	[100]	[1$\bar{1}$0]	[111]
ideal strength (GPa)	7.17	7.54	9.64	15.0	12.9	14.1
failure strain	0.288	0.358	0.346	0.232	0.184	0.242

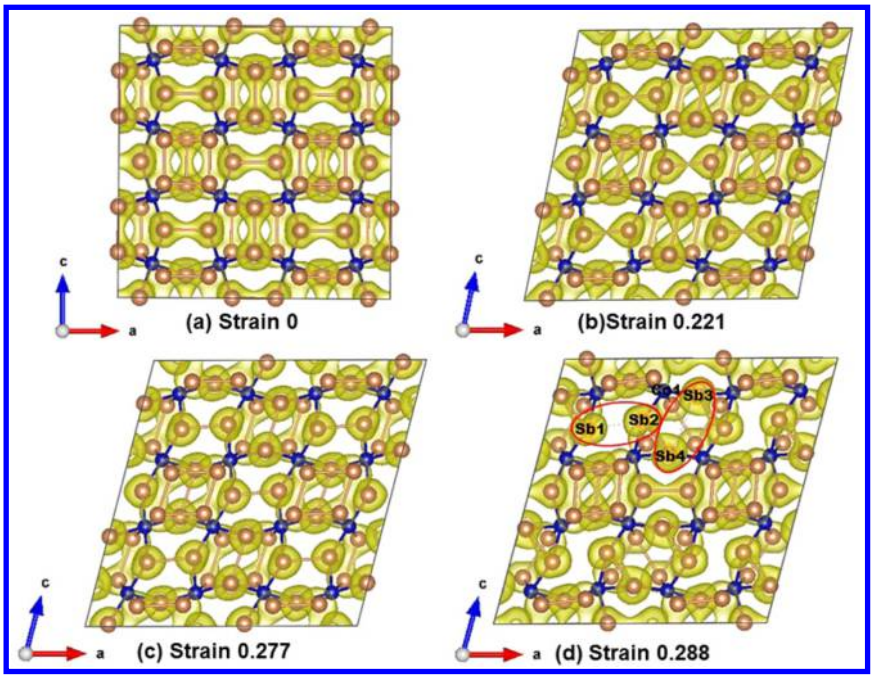

Figure 3. Calculated atomic positions combined with isosurfaces of the electron localization function (ELF) for shear loads along the (100)/⟨001⟩ slip system: (a) strain 0 corresponds to the initial stage, (b) strain 0.221 corresponds to the ideal strength, (c) strain 0.277 is before failure strain, and (d) failure strain is 0.288. The red circles highlight the key changes at this stage. The Co and Sb atoms are represented by blue and brown balls, respectively, and the ELF is represented by the shallow yellow regions.

monotonically, suggesting bond softening in the system, which corresponds to a "yielding" process. Then, at some point, the stress drops suddenly, indicating that the softening bond can no longer resist the external deformation, leading to bond failure and structural collapse.

3.3. Atomistic Explanation on Brittle Failure of $CoSb_3$.

3.3.1. Shear Failure Mode. In order to understand the origin of the brittleness in $CoSb_3$, it is essential to understand the structural failure modes under various loading conditions. Figure 3 displays the atomic positions for shearing along the (100)/⟨001⟩ slip system. It also shows the isosurface (at the value of 0.70) of the electron localization function (ELF), which analyzes the covalent bonding and lone pair formation.[35,36] As the applied strain increases to 0.221, all bonds stretch continuously, and the ELF shows that the Sb1−Sb2 and Sb3−Sb4 covalent bonds still share pairs of electrons. There is no bond breaking at this stage, and the structure (Sb-rings and Co−Sb frameworks) uniformly resists the shear deformation, resulting in the monotonous increase of stress. As the strain increases further to 0.277, the structure deforms further while the ELFs in the Sb1−Sb2 and Sb3−Sb4 bonds gradually move to the Sb atoms. This shows that the bonding electrons move toward the Sb atoms, suggesting that these bonds and Sb-rings are softening. Consequently, the stress decreases gradually with increasing strain. At strain of 0.288, the stress drops abruptly while the Sb1−Sb2 and Sb3−Sb4 bonds

DOI: 10.1021/acs.chemmater.5b02268
Chem. Mater. 2015, 27, 6329−6336

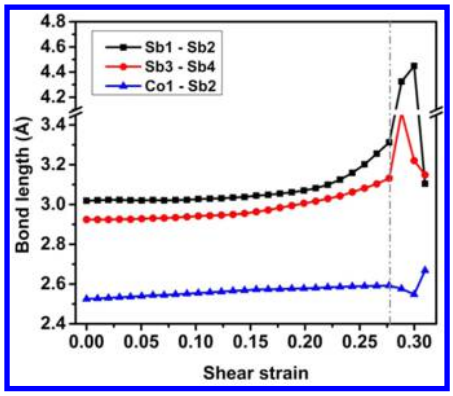

Figure 4. Average bond lengths (Sb1−Sb2, Sb3−Sb4, and Co1−Sb2 bonds marked in Figure 3) with the increasing shear strain along the (100)/⟨001⟩ slip system. The gray dashed line represents the strain before failure.

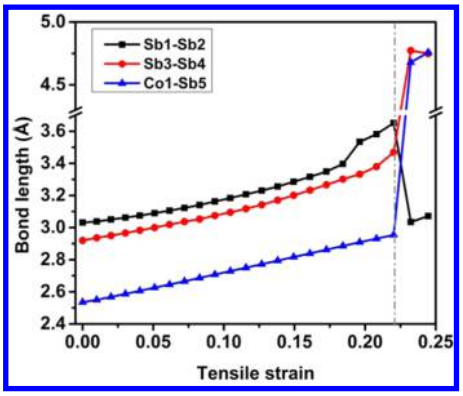

Figure 6. Average bond lengths (Sb1−Sb2, Sb3−Sb4, and Co1−Sb5 bonds marked in Figure 5) with the increasing tensile strain along the [100] tension system. The gray dashed line represents the strain before failure.

break, leading to deconstruction of the Sb-rings and structural failure.

Similarly, the failure modes along the (001)/⟨110⟩ and (111)/⟨1$\bar{1}$0⟩ slip systems also indicate that the deconstruction of Sb-rings and the collapse of Co−Sb frameworks lead to the structural failure. The detailed analyses are shown in Figures S1−S4.

To better understand the nature of the failure process for shearing along the (100)/⟨001⟩ slip system, the average bond lengths (Sb1−Sb2, Sb3−Sb4, and Co1−Sb2 bonds marked in Figure 3) are shown in Figure 4. As the strain increases to 0.221, all bonds increase slowly. With further increased strain, the Sb1−Sb2 and Sb3−Sb4 bonds stretch rapidly, indicating softening of the Sb-rings. However, the Co1−Sb2 bond is slightly stretched, indicating that the rigidity of the Co−Sb framework does not weaken much. At the failure strain of 0.288, we find that the Sb1−Sb2 and Sb3−Sb4 bond lengths increase steeply, suggesting breaking of the Sb-rings. However, the Co1−Sb2 bond length decreases only a little, indicating that the Co−Sb frameworks remain stable. The bond length

Table 3. Critical Bond Lengths (in Å) in $CoSb_3$ at the Strain Corresponding to the Ideal Strength

		bond		
		(short) Sb−Sb	(long) Sb−Sb	Co−Sb
		equilibrium length		
		2.90	3.03	2.53
shear	(001)/⟨100⟩	3.03	3.10	2.58
	(001)/⟨110⟩	2.97	3.19	2.63
	(111)/⟨1$\bar{1}$0⟩	3.05	3.17	2.66
tension	[100]	3.27	3.35	2.86
	[1$\bar{1}$0]	3.07	3.34	2.72
	[111]	3.02	3.15	2.93

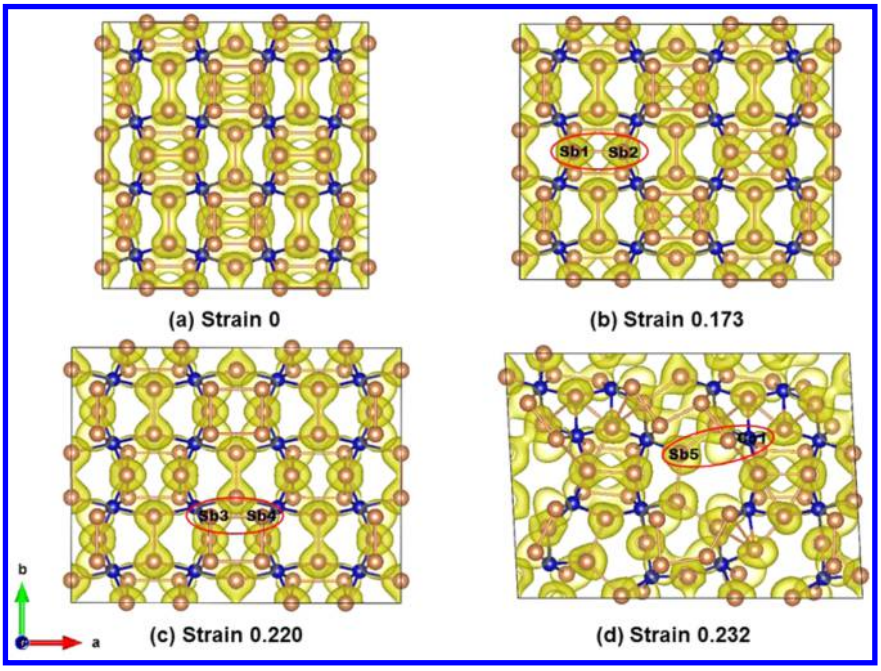

Figure 5. Calculated atomic positions combined with isosurfaces (at 0.70) of the electron localization function (ELF) for tensile loads along the [100] tension system: (a) strain 0 corresponds to the initial stage, (b) strain 0.173 corresponds to the ideal strength, (c) strain 0.220 is before failure strain, and (d) failure strain is 0.232.

DOI: 10.1021/acs.chemmater.5b02268
Chem. Mater. 2015, 27, 6329−6336

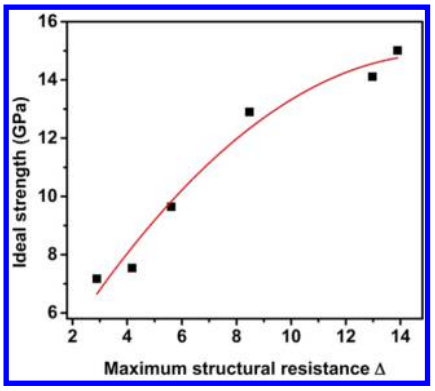

Figure 7. Predicted ideal strength as a function of the proposed "maximum structural resistance Δ" in $CoSb_3$. The red line guides the eye.

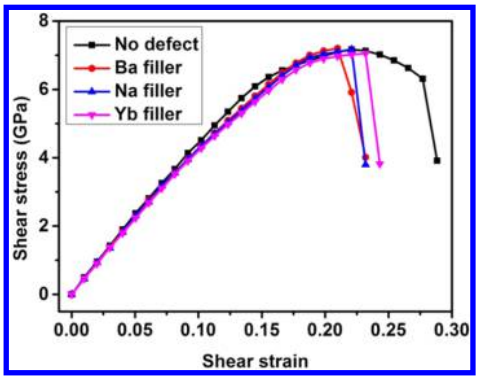

Figure 8. Calculated stress vs strain of filled $CoSb_3$ under (001)/⟨100⟩ shear loading.

changes clearly show that breaking of the Sb−Sb bonds (long Sb1−Sb2 and short Sb3−Sb4 bonds) leads to the structural failure. Prior to structural failure, the Sb1−Sb2 bond stretches from 3.03 to 3.31 Å, an increase of 9.24%. The Sb3−Sb4 bond increases by 7.89% from 2.90 to 3.13 Å. The Co1−Sb2 bond stretches much less, changing only from 2.53 to 2.58 Å, an increase of 1.98%.

3.3.2. Tensile Failure Mode. Figures 5 and 6 show the structures and average bond lengths as a function of [100] tension. The structure expands continuously along the [100] direction while shrinking along the other two directions (Poisson ratio of 0.223) until failure. At 0.173 strain, the Sb1−Sb2 bond has softened, which is shown clearly from the separated ELF in the Sb1−Sb2 bond, indicating that the rigidity of the Sb-rings has started to soften, even though they maintain the ideal rectangular shape. As the strain increases to 0.220, the Sb3−Sb4 bond softens, indicating additional Sb-ring softening. At 0.232 strain, the Sb3−Sb4 and Co1−Sb5 bonds break, leading to deconstruction of the Sb-rings and collapse of Co−Sb frameworks and stress relaxation.

The failure modes along [1$\bar{1}$0] and [111] tension systems shown in Figures S5−S8 also indicate that the breaking of Sb-rings and Co−Sb frameworks result in the structural failure. In Figure 6, the Sb1−Sb2 and Sb3−Sb4 bonds stretch slowly until a strain of 0.172. Then, the bond distance extension rate increases gradually, leading to softening of Sb-rings until bond failure. We observe that Co1−Sb5 bond deforms uniformly before the failure, with an increase in length by 17.00%, illustrating that the Co−Sb framework always maintains strong rigidity until failure. The Sb1−Sb2 and Sb3−Sb4 bond lengths change from 3.03 to 3.65 Å and from 2.90 to 3.47 Å, with an increase of 20.46% and 19.66% respectively. The Co1−Sb5 bond length changes from 2.53 to 2.96 Å, with an increase of 17.00%.

3.4. Structural Effects on the Ideal Strength. It is well-known that the ideal strength plays an important role in determining the reliability of brittle materials.[23,24] The ideal strength reflects the structural resistance limitation on external deformation. The deformations of Sb-rings and Co−Sb frameworks are indicated by the Sb−Sb and Co−Sb bond lengths, respectively. Table 3 lists the critical bond lengths in $CoSb_3$ at the strain corresponding to the ideal strength under shear and tensile loadings. We find that the deformation of the Co−Sb bond is closely related to the ideal strength. For example, along the (001)/⟨100⟩ slip system, the Co−Sb bond has the smallest deformation (2.53−2.58 Å) compared with other loading systems, and the system has the lowest ideal strength (7.17 GPa). Along [100] and [111] tension systems, the Co−Sb bond has the largest deformations (2.53−2.86 and 2.53−2.93 Å), and systems have the highest ideal strength (15.01 and 14.11 GPa). This indicates that Co−Sb bond deformation is important to the ideal strength. In other words, the rigidity of Co−Sb frameworks is much stronger than that of the Sb-rings. This is consistent with the force constant of the Co−Sb bond being larger than that of the long Sb−Sb bond.[37] More importantly, there are twice as many Co−Sb bonds as Sb−Sb bonds in $CoSb_3$ (48 Co−Sb bonds and 24 Sb−Sb bonds per unit cell), which further indicates that the Co−Sb bond is responsible for the ideal strength. However, when the Co−Sb bonds are deformed significantly, the Sb−Sb bonds

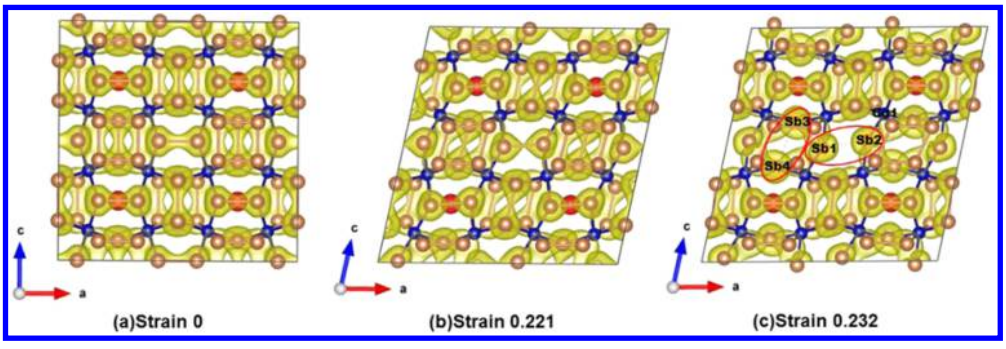

Figure 9. Atomic positions combined with the ELF (at the value of 0.7) along the (100)/⟨001⟩ slip $Na_4Co_{32}Sb_{96}$ system: (a) strain 0 corresponds to the initial stage, (b) strain 0.221 corresponds to the ideal strength, and (c) failure strain is 0.232. Red balls represent the Na atoms.

DOI: 10.1021/acs.chemmater.5b02268
Chem. Mater. 2015, 27, 6329−6336

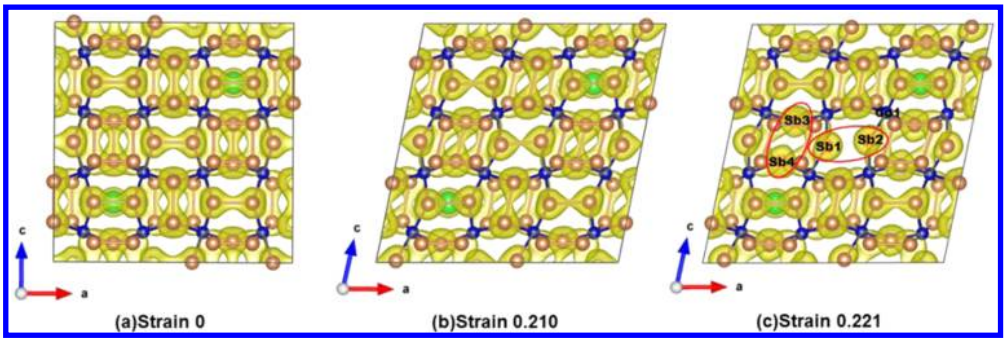

Figure 10. Atomic positions combined with the ELF (at the value of 0.7) along the (100)/⟨001⟩ slip $Ba_2Co_{32}Sb_{96}$ system: (a) strain 0 corresponds to the initial stage, (b) strain 0.210 corresponds to the ideal strength, and (c) failure strain is 0.221. Green balls represent the Ba atoms.

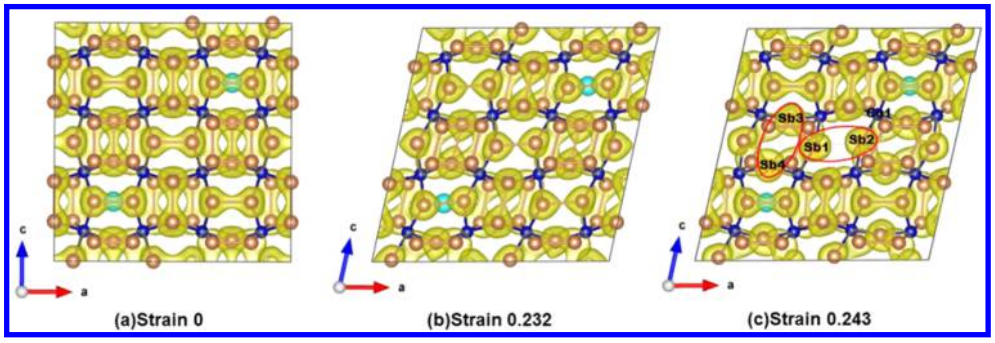

Figure 11. Atomic positions combined with the ELF (at the value of 0.7) along the (100)/⟨001⟩ slip $Yb_2Co_{32}Sb_{96}$ system: (a) strain 0 corresponds to the initial stage, (b) strain 0.232 corresponds to the ideal strength, and (c) failure strain is 0.243. Cyan balls represent the Yb atoms.

Table 4. Change of Typical Bond Lengths (in Å) in Filled and Unfilled $CoSb_3$, from No Strain to the Strain Corresponding to the Ideal Strength

compound	(short) Sb−Sb	(long) Sb−Sb	Co−Sb
$Na_4Co_{32}Sb_{96}$	2.91−3.01	3.00−3.06	2.52−2.57
$Ba_2Co_{32}Sb_{96}$	2.93−3.03	3.00−3.04	2.54−2.60
$Yb_2Co_{32}Sb_{96}$	2.93−3.05	3.04−3.12	2.54−2.59
$Co_{32}Sb_{96}$	2.90−3.03	3.03−3.10	2.53−2.58

have much larger deformation leading to larger ideal strength, as observed in the [100] and [111] tension systems.

In order to investigate quantitatively the structural effect on the ideal strength, we propose the "maximum structural resistance (Δ)" to evaluate structural resistance limitation on external deformation. The Δ is defined in the following equation, where i represents the bond type in the system, k_i is the force constant of the i bond, n_i is the weight of the i bond, L^i is the i bond length at the strain that corresponds to the ideal strength, and L_0^i is the i bond length at the equilibrium state (no strain).

$$\Delta = \sum_i k_i n_i (L^i - L_0^i)$$

For $CoSb_3$, the i bond corresponds to the Co−Sb bond, the long Sb−Sb bond, and the short Sb−Sb bond, respectively. The bond force constant k_i is chosen from ref 37. The bond weight n_i is determined by the number of i bonds. Since there are 48 Co−Sb, 12 long Sb−Sb, and 12 short Sb−Sb bonds in the unit cell, $n_{Co-Sb} = 4$, $n_{long\ Sb-Sb} = 1$, and $n_{short\ Sb-Sb} = 1$. L^i and L_0^i are listed in Table 3. Figure 7 plots the relationship between predicted shear or tensile ideal strength and corresponding maximum structural resistance Δ. This shows clearly the correlation of the ideal strength with Δ. Shearing along the (001)/⟨100⟩ slip system has the smallest Δvalue (2.88), representing the weakest resistance on external deformation and leading to the lowest ideal strength. The calculated kn (28.2) of the Co−Sb bond is much larger than that of the short Sb−Sb bond (7.7) and the long Sb−Sb bond (5.4), suggesting that the Co−Sb bond contributes 4 or 5 times more in determining Δ compared with Sb−Sb bonds. This verifies our conclusion that the Co−Sb bond deformation dominates the ideal strength.

3.5. Effect on Mechanics of $CoSb_3$ by Filling. Here, we used the single crystal to examine the intrinsic brittle failure mechanism of $CoSb_3$. For the polycrystal in which grain boundaries are important for failure, we expect that the initial failure mechanism at the grain boundary region is related to that of the single crystal.[38] To enhance the mechanical strength, we suggest that the Sb-ring structures be stabilized. Filling the intrinsic cages with impurity atoms such as rare earth elements (Yb, La, Ce, and Eu), alkaline earth elements (Ba, Ca, and Sr), and other elements (Na, K, and In) has been confirmed to increase the zT value of $CoSb_3$.[6,9,39−47] Herein, we examine the influence of a single-filling atom (Na, Ba, or Yb) on the mechanical behavior of $CoSb_3$. We choose the most plausible slip system, (100)/⟨001⟩. The model of filled $CoSb_3$ is $Na_4Co_{32}Sb_{96}$, $Ba_2Co_{32}Sb_{96}$, and $Yb_2Co_{32}Sb_{96}$ respectively, and all of them have the same carriers ($\sim 10^{21}$ cm^{-3}). Experimentally, doped n-type $CoSb_3$-based material has the highest ZT value for carrier concentrations of $\sim 0.5 \times 10^{21}$ cm^{-3} at room temperature.[48] Thus, we modeled with $Na_4Co_{32}Sb_{96}$, $Ba_2Co_{32}Sb_{96}$, and $Yb_2Co_{32}Sb_{96}$, all of which have carrier concentrations of $\sim 10^{21}$ cm^{-3}.

Figure 8 plots the stress−strain responses of filled $CoSb_3$ under (001)/⟨100⟩ shear loading. Figures 9−11 show the atomic configuration of filled $CoSb_3$ (Na, Ba, and Yb), respectively. This shows clearly that there is no obvious effect

DOI: 10.1021/acs.chemmater.5b02268
Chem. Mater. 2015, 27, 6329−6336

on the mechanics of $CoSb_3$ for all 3 filling atoms. Indeed, they show the same failure mode, which again is attributed to deconstruction of the Sb-rings caused by the failure of short Sb1−Sb2 and long Sb3−Sb4 bonds. Both filled and unfilled $CoSb_3$ have nearly the same ideal strength (~7.10 GPa). Table 4 shows that the change in the critical Co−Sb and Sb−Sb bond lengths from no strain to the strain corresponding to the ideal strength are nearly the same for all three cases, leading to nearly the same maximum structural resistance Δ (~2.88). This explains why they have the same ideal strength. Compared with filled $CoSb_3$, it seems that the stress in unfilled $CoSb_3$ increases smoothly to the ideal strength and then decreases gradually until failure, suggesting a "yielding" feature, which is due to structural integrity which uniformly resists the external shear deformation in unfilled $CoSb_3$. Filling atoms into the intrinsic cage changes the structural symmetry. Even though the change is very small, it still breaks the high consistency of structural integrity in resisting the shear deformation at large strains. Thus, the "yielding" stage disappeared in unfilled $CoSb_3$. Compared with the failure mode of unfilled $CoSb_3$, we find that the location of Sb−Sb bond failure changes, as shown in Figures 3 and 9−11. The Ba−Sb, Na−Sb, and Yb−Sb bond lengths are 3.47, 3.42, and 3.43 Å, respectively. Such long bonds indicate that the A−Sb bond (A = Ba, Na, and Yb) between A filler and Sb-rings must be a weak covalent bond in filled $CoSb_3$. However, the weak interaction between the doped atom and Sb atoms slightly enhances the structural rigidity of Sb-rings, leading to breaking of the unfilled Sb-rings, as shown in Figures 9−11. Due to the filling limitation in $CoSb_3$,[49] it is difficult to enhance the rigidity of all the Sb-rings. On the other hand, the weak A−Sb bond (A = filled atom) has little effect on Sb-rings. Thus, filler atoms have little influence on the fracture strength of $CoSb_3$.

4. CONCLUSIONS

We used density functional theory to study the intrinsic mechanical behavior of $CoSb_3$ under various shear and tensile loading conditions with the focus on the nature of the brittleness. Among all shear and tensile systems, $CoSb_3$ has the lowest ideal strength (7.17 GPa) under (001)/⟨100⟩ shear load, which we attribute to the Co−Sb bond deformation. The Sb-rings are always easier to soften than the Co−Sb frameworks because of the softer Sb−Sb bond. We find that the deconstruction of Sb-rings and the collapse of Co−Sb frameworks result in structural failure. Filling atoms (Na, Ba, and Yb) into the intrinsic cages of $CoSb_3$ has no obvious effect on the failure mechanism of $CoSb_3$ because the atom filler has little effect on the Sb-rings.

■ ASSOCIATED CONTENT

Supporting Information

The Supporting Information is available free of charge on the ACS Publications website at DOI: 10.1021/acs.chemmater.5b02268.

The shear failure mode of $CoSb_3$ along the (001)/⟨110⟩ and (111)/⟨1$\bar{1}$0⟩ slip system and tensile failure mode of $CoSb_3$ along the [1$\bar{1}$0] and [111] tension system, respectively. (PDF)

■ AUTHOR INFORMATION

Corresponding Authors

*E-mail: jeff.snyder@northwestern.edu.

*E-mail: wag@wag.caltech.edu.

*E-mail: zhangqj@whut.edu.cn.

Author Contributions

§G.L. and Q.A. contributed equally to this work.

Notes

The authors declare no competing financial interest.

■ ACKNOWLEDGMENTS

This work is partially supported by National Basic Research Program of China (973-program) under Project No. 2013CB632505, the 111 Project of China under Project No. B07040, Materials Project by Department of Energy Basic Energy Sciences Program under Grant No. EDCBEE, DOE Contract DE-AC02-05CH11231, National Natural Science Foundation of China (No. 11302156), and China Postdoctoral Science Foundation (408-32200031). Q.A. and W.A.G. were supported by the Defense Advanced Research Projects Agency (W31P4Q-13-1-0010, program manager, Judah Goldwasser).

■ REFERENCES

(1) Snyder, G. J.; Toberer, E. S. Complex Thermoelectric Materials. *Nat. Mater.* **2008**, *7*, 105−114.

(2) Nolas, G. S.; Morelli, D. T.; Tritt, T. M. Skutterudites: A Phonon-Glass-Electron Crystal Approach to Advanced Thermoelectric Energy Conversion Applications. *Annu. Rev. Mater. Sci.* **1999**, *29*, 89−116.

(3) Zhou, X. Y.; Wang, G. W.; Guo, L. J.; Chi, H.; Wang, G. Y.; Zhang, Q. F.; Chen, C. Q.; Thompson, T.; Sakamoto, J.; Dravid, V. P.; Cao, G. Z.; Uher, C. Hierarchically Structured TiO2 for Ba-Filled Skutterudite with Enhanced Thermoelectric Performance. *J. Mater. Chem. A* **2014**, *2*, 20629−20635.

(4) Ballikaya, S.; Uher, C. Enhanced Thermoelectric Performance of Optimized Ba, Yb Filled and Fe Substituted Skutterudite Compounds. *J. Alloys Compd.* **2014**, *585*, 168−172.

(5) Rull-Bravo, M.; Moure, A.; Fernandez, J. F.; Martin-Gonzalez, M. Skutterudites as Thermoelectric Materials: Revisited. *RSC Adv.* **2015**, *5*, 41653−41667.

(6) Tang, Y. L.; Qiu, Y. T.; Xi, L. L.; Shi, X.; Zhang, W. Q.; Chen, L. D.; Tseng, S. M.; Chen, S. W.; Snyder, G. J. Phase Diagram of In−Co−Sb System and Thermoelectric Properties of In-Containing Skutterudites. *Energy Environ. Sci.* **2014**, *7*, 812−819.

(7) Shi, X.; Yang, J.; Salvador, J. R.; Chi, M. F.; Cho, J. Y.; Wang, H.; Bai, S. Q.; Yang, J. H.; Zhang, W. Q.; Chen, L. D. Multiple-Filled Skutterudites: High Thermoelectric Figure of Merit through Separately Optimizing Electrical and Thermal Transports. *J. Am. Chem. Soc.* **2011**, *133*, 7837−7846.

(8) Uher, C. In *Handbook of Thermoelectrics: Macro to Nano*; Rowe, D. M., Ed.; CRC Press: Boca Raton, FL, 2006; Chapter 34, pp 1−17.

(9) Zhao, W. Y.; Wei, P.; Zhang, Q. J.; Dong, C. L.; Liu, L. S.; Tang, X. F. Enhanced Thermoelectric Performance in Barium and Indium Double-Filled Skutterudite Bulk Materials via Orbital Hybridization Induced by Indium Filler. *J. Am. Chem. Soc.* **2009**, *131*, 3713−3720.

(10) Rogl, G.; Grytsiv, A.; Rogl, P.; Peranio, N.; Bauer, E.; Zehetbauer, M.; Eibl, O. n-Type Skutterudites $(R,Ba,Yb)_yCo_4Sb_{12}$ (R = Sr, La, Mm, DD, SrMm, SrDD) Approaching ZT ≈ 2.0. *Acta Mater.* **2014**, *63*, 30−43.

(11) El-Genk, M. S.; Saber, H. H.; Caillat, T.; Sakamoto, J. Tests Results and Performance Comparisons of Coated and Un-Coated Skutterudite Based Segmented Unicouples. *Energy Convers. Manage.* **2006**, *47*, 174−200.

(12) Zhao, D. G.; Geng, H. R.; Chen, L. D. Microstructure Contact Studies for $CoSb_3$ Thermoelectric Devices. *Int. J. Appl. Ceram. Technol.* **2012**, *9*, 733−741.

(13) Bae, K. H.; Choi, S. M.; Kim, K. H.; Choi, H. S.; Seo, W. S.; Kim, I. H.; Lee, S.; Hwang, H. J. Power-Generation Characteristics After Vibration and Thermal Stresses of Thermoelectric Unicouples

DOI: 10.1021/acs.chemmater.5b02268
Chem. Mater. 2015, 27, 6329−6336

with $CoSb_3$ /Ti/Mo(Cu) Interfaces. *J. Electron. Mater.* **2015**, *44*, 2124−2131.
(14) Rogl, G.; Rogl, P. Mechanical Properties of Skutterudites. *Sci. Adv. Mater.* **2011**, *3*, 517−538.
(15) Ravi, V.; Firdosy, S.; Caillat, T.; Lerch, B.; Calamino, A.; Pawlik, R.; Nathal, M.; Sechrist, A.; Buchhalter, J.; Nutt, S. Mechanical Properties of Thermoelectric Skutterudites. *AIP Conf. Proc.* **2008**, *969*, 656−662.
(16) Ruan, Z. W.; Liu, L. S.; Zhai, P. C.; Wen, P. F.; Zhang, Q. J. Low-Cycle Fatigue Properties of CoSb3-Based Skutterudite Compounds. Low-Cycle Fatigue Properties of $CoSb_3$ -Based Skutterudite Compounds. *J. Electron. Mater.* **2010**, *39*, 2029−2033.
(17) Schmidt, R. D.; Case, E. D.; Ni, J. E.; Sakamoto, J. S.; Trejo, R. M.; Lara-Curzio, E.; et al. The temperature Dependence of Thermal Expansion for p-type $Ce_{0.9}Fe_{3.5}Co_{0.5}Sb_{12}$ and n-type $Co_{0.95}Pd_{0.05}Te_{0.05}Sb_3$ Skutterudite Thermoelectric Materials. *Philos. Mag.* **2012**, *92*, 1261−1286.
(18) Yang, X. Q.; Zhai, P. C.; Liu, L. S.; Zhang, Q. J. Thermodynamic and Mechanical Properties of Crystalline $CoSb_3$: A Molecular Dynamics Simulation Study. *J. Appl. Phys.* **2011**, *109*, 123517−123517−6.
(19) Li, W. J.; Li, G. D.; Yang, X. Q.; Liu, L. S.; Zhai, P. C. Influence of Nanopores on the Tensile/Compressive Mechanical Behavior of Crystalline $CoSb_3$: A Molecular Dynamics Study. *J. Electron. Mater.* **2015**, *44*, 1477−1482.
(20) Li, W.; Zhai, P.; Li, G.; Yang, X.; Liu, L. Molecular Dynamics Simulation on Mechanical Properties of Crystalline $CoSb_3$ with Nanopores. *Mater. Res. Innovations* **2014**, *18*, S4-106−S4-109.
(21) Morelli, D. T.; Caillat, T.; Fleurial, J. P.; Borshchevsky, A.; Vandersande, J.; Chen, B.; Uher, C. Low-Temperature Transport Properties of p-type $CoSb_3$. *Phys. Rev. B: Condens. Matter Mater. Phys.* **1995**, *51*, 9622−9628.
(22) An, Q.; Goddard, W. A.; Cheng, T. Atomistic Explanation of Shear-Induced Amorphous Band Formation in Boron Carbide. *Phys. Rev. Lett.* **2014**, *113*, 095501-1−095501-5.
(23) Ogata, S.; Li, J.; Yip, S. Ideal Pure Shear Strength of Aluminum and Copper. *Science* **2002**, *298*, 807−811.
(24) Roundy, D.; Krenn, C. R.; Cohen, M. L.; Morris, J. W. Ideal Shear Strengths of fcc Aluminum and Copper. *Phys. Rev. Lett.* **1999**, *82*, 2713−2716.
(25) Kresse, G.; Furthmuller, J. Efficiency of ab-initio Total Energy Calculations for Metals and Semiconductors Using a Plane-Wave Basis Set. *Comput. Mater. Sci.* **1996**, *6*, 15−50.
(26) Kresse, G.; Furthmuller, J. Efficient Iterative Schemes for ab initio Total-Energy Calculations Using a Plane-Wave Basis Set. *Phys. Rev. B: Condens. Matter Mater. Phys.* **1996**, *54*, 11169−11186.
(27) Kresse, G.; Joubert, D. From Ultrasoft Pseudopotentials to the Projector Augmented-Wave Method. *Phys. Rev. B: Condens. Matter Mater. Phys.* **1999**, *59*, 1758−1775.
(28) Schmidt, T.; Kliche, G.; Lutz, H. D. Structure Refinement of Skutterudite-Type Cobalt Triantimonide, $CoSb_3$. *Acta Crystallogr., Sect. C: Cryst. Struct. Commun.* **1987**, *43*, 1678−1679.
(29) Kim, H.; Kaviany, M.; Thomas, J. C.; Van der Ven, A.; Uher, C.; Huang, B. L. Structural Order-Disorder Transitions and Phonon Conductivity of Partially Filled Skutterudites. *Phys. Rev. Lett.* **2010**, *105*, 265901-1−265901-4.
(30) Guo, R. Q.; Wang, X. J.; Huang, B. L. Thermal Conductivity of Skutterudite $CoSb_3$ from First Principles: Substitution and Nano-engineering Effects. *Sci. Rep.* **2015**, *5*, 7806−7806−9.
(31) Magan, G. D. Good Thermoelectrics. *Solid State Phys.* **1997**, *51*, 81−157.
(32) Chung, D. H. Elastic Moduli of Single-Crystal and Polycrystalline MgO. *Philos. Mag.* **1963**, *8*, 833−841.
(33) Keppens, V.; Mandrus, D.; Sales, B. C.; Chakoumakos, B. C.; Dai, P.; Coldea, R.; Maple, M. B.; Gajewski, D. A.; Freeman, E. J.; Bennington, S. Localized Vibrational Modes in Metallic Solids. *Nature* **1998**, *395*, 876−878.
(34) Rotter, M.; Rogl, P.; Grytsiv, A.; Wolf, W.; Krisch, M.; Mirone, A. Lattice Dynamics of Skutterudites: Inelastic x-Ray Scattering on $CoSb_3$. *Phys. Rev. B: Condens. Matter Mater. Phys.* **2008**, *77*, 144301-1−144301-5.
(35) Becke, A. D.; Edgecombe, K. E. A Simple Measure of Electron Localization in Atomic and Molecular Systems. *J. Chem. Phys.* **1990**, *92*, 5397−5403.
(36) Silvi, B.; Savin, A. Classification of Chemical Bonds Based on Topological Analysis of Electron Localization Functions. *Nature* **1994**, *371*, 683−686.
(37) Feldman, J. L.; Singh, D. J. Lattice Dynamics of Skutterudites: First-Principles and Model Calculations for $CoSb_3$. *Phys. Rev. B: Condens. Matter Mater. Phys.* **1996**, *53*, 6273−6282.
(38) Inoue, H.; Akahoshi, Y.; Harada, S. Molecular Dynamics Simulation on Fracture Mechanisms of Nano-Scale Polycrystal under Static and Cyclic Loading. *J. Soc. Mater. Sci., Jpn.* **1995**, *44*, 95−99.
(39) Graff, J. W.; Zeng, X.; Dehkordi, A. M.; He, J.; Tritt, T. M. Exceeding the Filling Fraction Limit in $CoSb_3$ Skutterudite: Multi-Role Chemistry of Praseodymium Leading to Promising Thermoelectric Performance. *J. Mater. Chem. A* **2014**, *2*, 8933−8940.
(40) Fu, L. W.; Yang, J. Y.; Peng, J. Y.; Jiang, Q. H.; Xiao, Y.; Luo, Y. B.; Zhang, D.; Zhou, Z. W.; Zhang, M. Y.; Cheng, Y. D.; Cheng, F. Q. Enhancement of Thermoelectric Properties of Yb-Filled Skutterudites by An Ni-Induced "Core-Shell" Structure. *J. Mater. Chem. A* **2015**, *3*, 1010−1016.
(41) Mi, J. L.; Christensen, M.; Nishibori, E.; Iversen, B. B. Multitemperature Crystal Structures and Physical Properties of the Partially Filled Thermoelectric Skutterudites $M_{0.1}Co_4Sb_{12}$(M = La, Ce, Nd, Sm, Yb, and Eu). *Phys. Rev. B: Condens. Matter Mater. Phys.* **2011**, *84*, 064114-1−064114-12.
(42) Xi, L. L.; Yang, J.; Lu, C. F.; Mei, Z. G.; Zhang, W. Q.; Chen, L. D. Systematic Study of the Multiple-Element Filling in Caged Skutterudite $CoSb_3$. *Chem. Mater.* **2010**, *22*, 2384−2394.
(43) Rogl, G.; Grytsiv, A.; Rogl, P.; Bauer, E.; Hochenhofer, M.; Anbalagan, R.; Mallik, R. C.; Schafler, E. Nanostructuring of p- and n-Type Skutterudites Reaching Figures of Merit of Approximately 1.3 and 1.6, Respectively. *Acta Mater.* **2014**, *76*, 434−438.
(44) Li, D.; Yang, K.; Hng, H. H.; Qin, X. Y.; Ma, J. Electrical Transport and Thermoelectric Properties of Double fFilled Compounds $Ca_{0.1}Ce_xCo_4Sb_{12}$ at Low Temperatures. *J. Appl. Phys.* **2008**, *104*, 103720−103720−6.
(45) Cho, J. Y.; Ye, Z. X.; Tessema, M. M.; Salvador, J. R.; Waldo, R. A.; Yang, J.; Zhang, W. Q.; Yang, J. H.; Cai, W.; Wang, H. Thermoelectric Performance of p-Type Skutterudites $Yb_xFe_{4-y}Pt_ySb_{12}$ ($0.8 \leqslant x \leqslant 1$, y = 1 and 0.5). *J. Appl. Phys.* **2013**, *113*, 143708-1−143708-8.
(46) Pei, Y. Z.; Yang, J.; Chen, L. D.; Zhang, W.; Salvador, J. R.; Yang, J. H. Improving Thermoelectric Performance of Caged Compounds through Light-Element Filling. *Appl. Phys. Lett.* **2009**, *95*, 042101−042101−3.
(47) Yang, J.; Qiu, P.; Liu, R.; Xi, L.; Zheng, S.; Zhang, W.; Chen, L.; Singh, D. J.; Yang, J. H. Trends in Electrical Transport of p-Type Skutterudites RFe_4Sb_{12} (R = Na, K, Ca, Sr, Ba, La, Ce, Pr, Yb) from First-Principles Calculations and Boltzmann Transport Theory. *Phys. Rev. B: Condens. Matter Mater. Phys.* **2011**, *84*, 235205-1−235205-10.
(48) Tang, Y. L.; Hanus, R.; Chen, S. W.; Snyder, G. J. Solubility Design Leading to High Figure of Merit in Low-Cost Ce-$CoSb_3$ Skutterudites. *Nat. Commun.* **2015**, *6*, 7584−7584−7.
(49) Shi, X.; Zhang, W.; Chen, L. D.; Yang, J. Filling Fraction Limit for Intrinsic Voids in Crystals: Doping in Skutterudites. *Phys. Rev. Lett.* **2005**, *95*, 185503−185503−4.

DOI: 10.1021/acs.chemmater.5b02268
Chem. Mater. 2015, 27, 6329−6336